RSC Advances

PAPER

View Article Online
View Journal | View Issue

Cite this: *RSC Adv.*, 2022, **12**, 19101

Effect of rGO with $BaCuO_3$ perovskite on the thermal decomposition of AP and NTO†

Pragnesh N. Dave, * Riddhi Thakkar* and Ruksana Sirach

Received 13th February 2022
Accepted 6th June 2022

DOI: 10.1039/d2ra00953f

rsc.li/rsc-advances

In this study, the syntheses of a $BaCuO_3$ perovskite-structured oxide and rGO were conducted using a sol–gel method and ultrasonication process, respectively. Their physico-chemical characteristics were studied by powder X-ray diffraction (PXRD), Raman spectroscopy, and ultraviolet-visible (UV-vis) spectroscopy analyses. The perovskite type particles were found to present as a cubic crystal system with a crystal size in the range of 10–60 nm. Their catalytic performance was investigated using differential thermal analysis (DTA) measurements at varying heating rates *via* the thermal decomposition of ammonium perchlorate (AP) and 3-nitro-1,2,4-triazol-5-one (NTO). The kinetics and thermodynamics parameters, such as the average activation energy, pre-exponential factor, entropy, and Gibbs free energy, were also investigated, which showed a decrease in the decomposition peak temperature of AP and NTO in the presence of the catalysts rGO, $BaCuO_3$, and rGO + $BaCuO_3$ compared to pure AP and NTO.

1. Introduction

In a chemical propulsion system, ammonium perchlorate (AP) works as an oxidizer, while nitrotriazolone or 3-nitro-1,2,4-triazol-5-one (NTO) acts as insensitive high energetic materials that has potential for use as an oxidizer.[1–3] They are used in chemical reactions in rockets to release energy and produce large thrusts in short periods of time. The thermal decomposition behaviour of AP and NTO plays a major role in explosives formulations.[4–6] Their thermal properties can be improved by adding additives such as metal oxides,[7] metal ferrites,[8] and metal composites,[9] which work as a catalyst by accelerating the proton transfer mechanism during the thermolysis process. Previous studies have provided information about the nano size of the particles of catalysts highly influencing the decomposition process due to them having more active sites to boost catalytic performance in the thermal decomposition of the energetic oxidants AP and NTO.[10,11]

Perovskite type oxides and reduced graphene oxide (rGO) type materials have been widely used in the field of catalysis, fuel cells, and sensors due to them exhibiting excellent and attractive physico-chemical characteristics such as electrical, mechanical, and thermal properties.[12,13] The history of ABO_3 (where A and B are metal cations) type perovskites[14] and rGO[15] suggests that perovskite-structured oxides contain localized electrons and have stable structures, modified physico-chemical properties, and variation of metal replacement. Meanwhile, graphene oxide has characteristics such as hydrophobicity, a highly conducting nature, and thermal stability. Thus, these special advanced materials have been used in various fields, in applications such as energy devices, drug delivery, catalysis, and many more.[16–18] Nowadays, the perovskite oxide $BaCuO_3$ is widely used due to its easy preparation, chemical stability, lower cost, and higher vibrational and electrical properties compared with other perovskite oxides.[19]

Herein, a wet chemical method was used to prepare perovskite-structured transition metal doped oxide $BaCuO_3$, while GO was reduced using an ultrasonication process. The catalytic effect that rGO, $BaCuO_3$, and $BaCuO_3$ + rGO have on the thermal decomposition of AP and NTO were briefly studied.

2. Experimental section

2.1. Synthesis of the perovskite oxide $BaCuO_3$

In the synthesis of the perovskite oxide $BaCuO_3$, a citrate-EDTA wet chemical complexing sol–gel method[20] was followed. The starting chemicals were citric acid monohydrate, barium nitrate, cupric(II) nitrate trihydrate, and ethylenediamine tetra-acetic acid (EDTA) di-sodium salt dihydrate, procured from Loba Chemie. Here, $Ba(NO_3)_2$ and $Cu(NO_3)_2 \cdot 3H_2O$ were in a 1 : 1 molar ratio, while the chelating agents EDTA and citric acid were in a 1 : 2 molar ratio, with both sets of reagents mixed together to obtain mixed solutions. A solution of NH_4OH was used to regulate the pH of the above mixed solution to ~6. The solutions were then heated at 100 °C under continuous stirring to obtain a viscous gel that was heated at 70 °C for 2 h in an oven to convert it to black powder *via* combustion in open air. Finally, the perovskite powder was calcined at 700 °C for 4 h to remove

Department of Chemistry, Sardar Patel University, Gujarat-388120, India. E-mail: Pragnesh7@yahoo.com

† Electronic supplementary information (ESI) available. See https://doi.org/10.1039/d2ra00953f

residual organics and the $BaCuO_3$ perovskite-structured oxide was obtained.

2.2. Synthesis of reduced graphene oxide (rGO)

Graphene oxide (GO) was obtained from Sigma-Aldrich and used as received. The GO was dissolved in acetone and ultrasonicated for 40 min before carrying out thermal reduction[21] at 350 °C for 1 min in a tubular furnace to produce r-GO. The perovskite oxide $BaCuO_3$ and rGO in a 2 : 1 molar ratio were mixed in acetone and sonicated for 1 h, then filtered and dried in an oven overnight to produce a rGO + $BaCuO_3$ mixture.

2.3. Synthesis of the insensitive explosive nitrotriazolone (NTO)

The preparation steps of NTO were explained briefly in our published work.[7]

2.4. Sample preparation with AP and NTO for thermal analysis

The catalytic performance was checked using rGO + AP, $BaCuO_3$ + AP, and rGO$BaCuO_3$ + AP in a 97 : 3 weight ratio, while rGO + NTO, $BaCuO_3$ + NTO, and rGO$BaCuO_3$ + NTO in a 95 : 5 weight ratio, by mixing them *via* ultrasonication in a ultrasonic bath. The process took place by dissolving the materials in acetone and sonicating for 40 minutes, then filtering and drying them in an oven overnight to result in the catalytic compositions containing AP and NTO.

3. Physico-chemical characterization techniques

Powder X-ray diffraction (XRD) patterns of rGO and the perovskite were analyzed using a Rigaku Ultima IV powder X-ray diffractometer equipped with a CuKα (λ = 1.5406 Å) radiation source. A high-resolution field emission gun nano nova scanning electron microscope (450 Nova NanoSEM 450 FEI Ltd) was used to obtain high resolution images of rGO and the nanomaterial. The samples underwent electronic spectral analysis using a UV-160 Shimadzu Pte Ltd UV-visible spectrophotometer and vibrational spectral analysis was achieved using a LabRam Dilor spectrometer equipped with an Olympus microscope (HS BX40) and 532 nm wavelength laser source Raman instrument. The perovskite oxide $BaCuO_3$ and rGO were tested as excellent catalysts for the thermal decomposition of AP and NTO using a thermogravimetric analyser/differential thermal analyser (TGA/DTA) (TA (5000/2960) instruments, USA) at different heating rates of 5 °C min^{-1}, 10 °C min^{-1}, 15 °C min^{-1}, and 20°C min^{-1} in an aluminum pan.

4. Results and discussion

4.1. XRD analyses

Fig. 1 shows the powder XRD patterns of calcined perovskite-structured oxide $BaCuO_3$, rGO, and rGO + $BaCuO_3$. Herein, rGO showed a characteristic peak position between 2θ angles of 20° and 30°, suggesting that GO was completely reduced to a crystalline powder.[22] The perovskite structured oxide $BaCuO_3$ has a cubic crystal system in the $Pm\bar{3}m$ space group. The XRD crystalline phases of $BaCuO_3$ and rGO + $BaCuO_3$ were similar to each other, while the intensity for rGO + $BaCuO_3$ was observed to be higher, indicating its better crystallinity (Fig. 1). For the perovskite sample $BaCuO_3$, the crystalline size was found to be in the range of 8–45 nm, as calculated using the Debye–Scherrer method.[23] Here, the $BaCuO_3$ perovskite oxide was calcined at 700 °C temperature, thus decomposed oxides Ba_2O_3, CuO, $Ba_2(CuO_2)_3$, and BaO_2 phases were observed in its XRD pattern. The major characteristic diffraction peaks with Miller indices[23] are (103), (110), (210), (211), (105), (015), (114), (200), (020), (222), (320), (321), (123), (206), and (215), found between 2θ angles of 20 and 60°.

The morphology of synthesized rGO, the perovskite structured $BaCuO_3$, and rGO + $BaCuO_3$ nanomaterials were

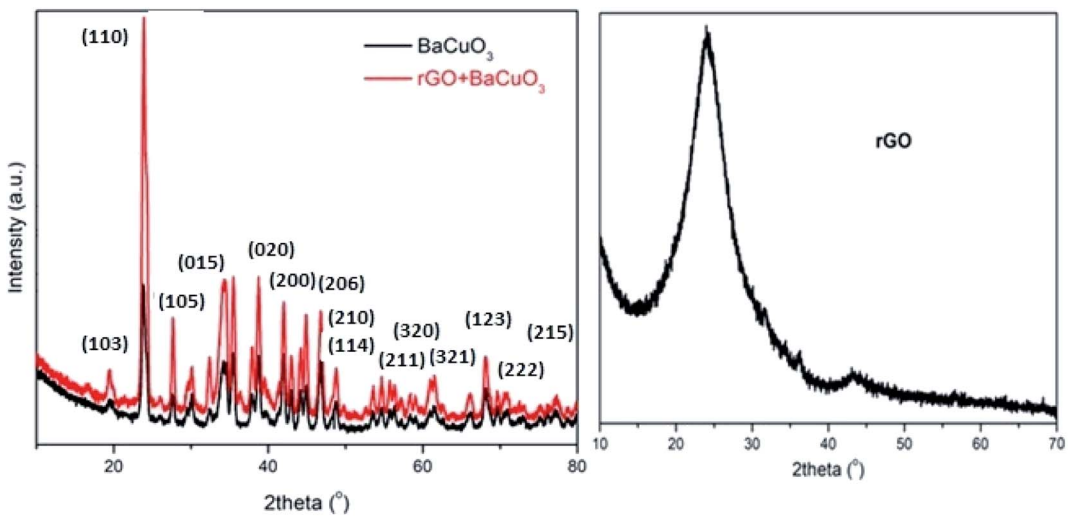

Fig. 1 Powder XRD of the rGO, $BaCuO_3$, and rGO + $BaCuO_3$ catalysts.

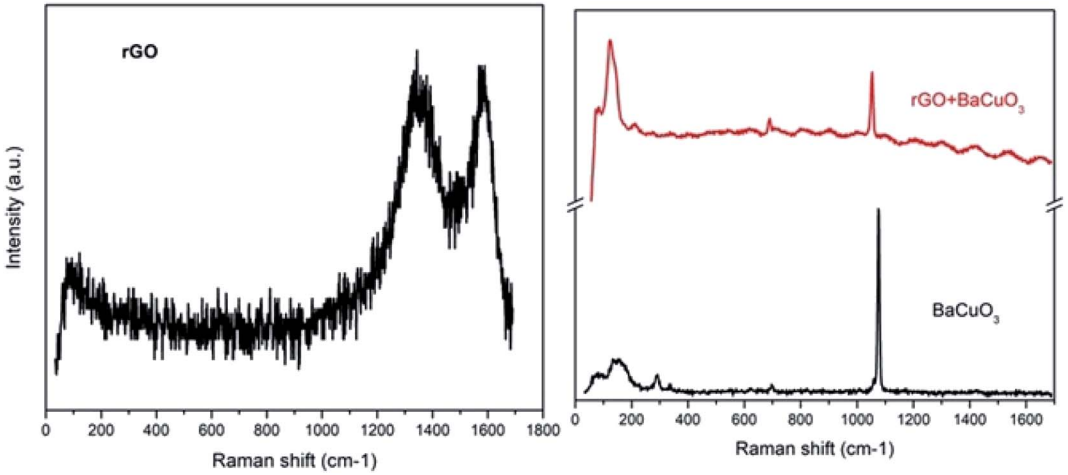

Fig. 2 Raman spectra of rGO, $BaCuO_3$, and rGO + $BaCuO_3$.

characterized by field emission gun (FEG)-SEM analysis. As shown in Fig 1S(a–c),† the $BaCuO_3$ nanoparticles were uniformly dispersed on the rGO sheets. Here, due to the long time period of sonication (~60 min) for the rGO + $BaCuO_3$ sample, it was observed that all of the $BaCuO_3$ nanoparticles were linked to rGO sheets, due to their strong interaction with the rGO sheets. Fig 1S(a)† shows that the graphene sheets have a hair-like texture. The high-resolution SEM images of the $BaCuO_3$ nanoparticles and their mixture with rGO, presented in Fig. 1S(b and c),† display a clear rectangular rod shape, agglomeration, polyhedra-like shape, and the presence of rGO sheets. Average particle sizes were calculated using ImageJ software and the particle size of $BaCuO_3$ was found to be in the range of ~8 to 25 nm. The SEM images of perovskite $BaCuO_3$ contained polyhedral grains with small and large particles that facilitated its smoother surface compared to the other samples.[23]

4.2. Raman spectroscopy analyses

The micro-Raman spectra of the thermally reduced graphene oxide (rGO), $BaCuO_3$, and rGO + $BaCuO_3$ are presented in Fig. 2. Due to structural defects in the rGO sample, two bands are observed, one is the G-band and the other is the D-band, attributed to the in-plane and out-of-plane vibrations of sp^2 bonded carbon atoms, respectively. In the Raman spectra of rGO, these bands were observed between 1200 and 1700 cm^{-1}. Significant Raman shifts in the D- and G-bands were observed at 1343 cm^{-1} and 1588 cm^{-1}, respectively, corresponding to the structural defects of the reduced graphene sheets. Thus, the value of I_D/I_G was 0.85%, related to the significant structural defects observed in the thermally synthesized rGO.

Moreover, the Raman scattering of a perovskite sample is very important to understand its structural defects and motion of oxygen. Herein, the Raman spectrum of $BaCuO_3$ shows vibrational modes of corresponding oxides between 50 to 800 cm^{-1} and the sharp peak between 1000 to 1200 cm^{-1} corresponds to phonon scattering. However, the Raman spectrum of rGO + $BaCuO_3$ shows a small Raman peak shift at a low wavenumber due to the longer bond length of the molecules, but the Raman shift of the thermally-prepared rGO was present with minor intensity due to the highly ultrasonicated intercalation of rGO with the perovskite structured oxide $BaCuO_3$, thus leading to lower polarizability of the molecules.[24]

4.3. UV-visible spectroscopy analyses

The electronic transition spectra of the perovskite-structured oxide and thermally-treated rGO are shown in Fig. 3. In the ultraviolet region, the $BaCuO_3$ and rGO + $BaCuO_3$ samples exhibited higher absorbance due to the presence of multiple electronic transition spectra, while pure rGO showed less absorbance and a spectral pattern that appeared flat due to the presence of unsaturated bonds in the rGO molecules.[22] Moreover, $BaCuO_3$ exhibited a higher band gap energy of 5.8 eV, calculated from its Tauc plot using the well-known formula reported in our previous studies[25] and an $(\alpha h\nu)^2$ *versus* energy ($h\nu$) curve was plotted, from which the direct optical band gap was obtained by extrapolating a straight line (Fig. 3).

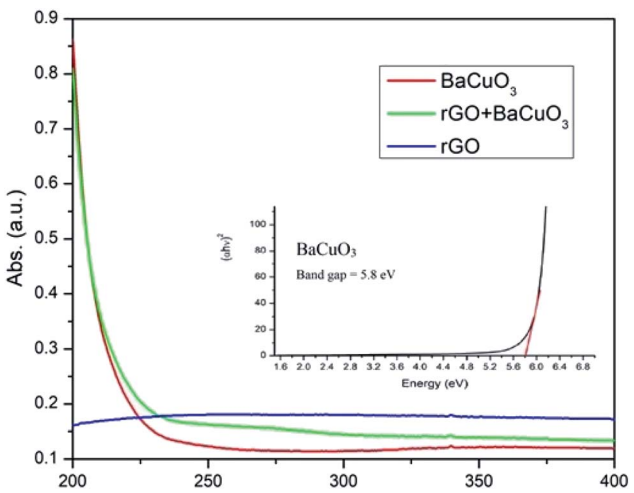

Fig. 3 Ultraviolet spectra of rGO, $BaCuO_3$, and rGO + $BaCuO_3$ and Tauc plot of $BaCuO_3$ (inset).

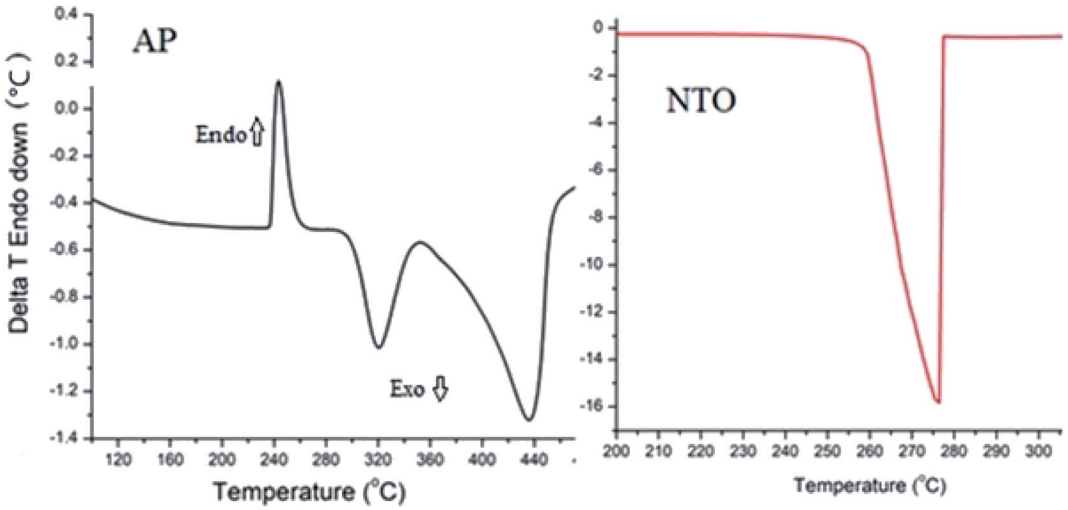

Fig. 4 Differential thermal thermographs of the AP and NTO energetic materials.

4.4. Thermal analyses of the thermolysis of ammonium perchlorate (NH_4ClO_4)

The catalytic performances of rGO, $BaCuO_3$, and rGO + $BaCuO_3$ for the thermal decomposition of AP were studied using DTA (differential thermal analysis) and the results are shown in Fig. 5. The thermograph of pure AP thermolysis is presented in Fig. 4, which shows a three-stage decomposition process; the first stage was an endothermic phase transition decomposition with a peak observed at around ~240 °C, while the remaining two stages corresponded to exothermic decomposition observed at around ~320 °C and ~435 °C, assigned as low-temperature decomposition (Ltd) and high-temperature decomposition (HTD), respectively. In Fig. 5, the thermographs of the catalytic decomposition of AP using 3 wt% of the catalysts rGO, $BaCuO_3$, and rGO + $BaCuO_3$ at two heating rates 10 °C min^{-1} and 20 °C min^{-1} show that the Ltd peak underwent significant changes, while only one exothermic peak was observed between 300 °C to 350 °C. As the heating rate increased, the decomposition peak temperature was also increased.

4.5. Catalytic mechanism

The perovskite-structured oxide $BaCuO_3$ is an oxygen active catalyst,[6] and rGO is a good electron acceptor.[26] The gases generated during the decomposition steps of ammonium perchlorate (AP) over $BaCuO_3$and $BaCuO_3$ + rGO are as follows:

$$3BaCuO_3 \rightarrow Ba_2(CuO_2)_3 + BaO + O_2 \quad (1)$$

$$BaCuO_3 + rGO \rightarrow BaCuO_3 + rGO\,(e^-) \quad (2)$$

$$NH_4ClO_4 \rightarrow NH_3 + HClO_4$$
$$\Downarrow$$
$$2HClO_4 \rightarrow \frac{1}{2}Cl_2 + H_2O + \frac{5}{2}O_2 + ClO_2 \quad (3)$$
$$2NH_3 + 2ClO_2 \rightarrow N_2O + Cl_2 + 3H_2O$$

When rGO + AP is heated, electrons rapidly transfer to rGO *via* a percolation mechanism, thus a broadening of the decomposition peak was observed at low temperature (Fig. 5). Also, once the mixture $BaCuO_3$ + AP is heated, the perovskite

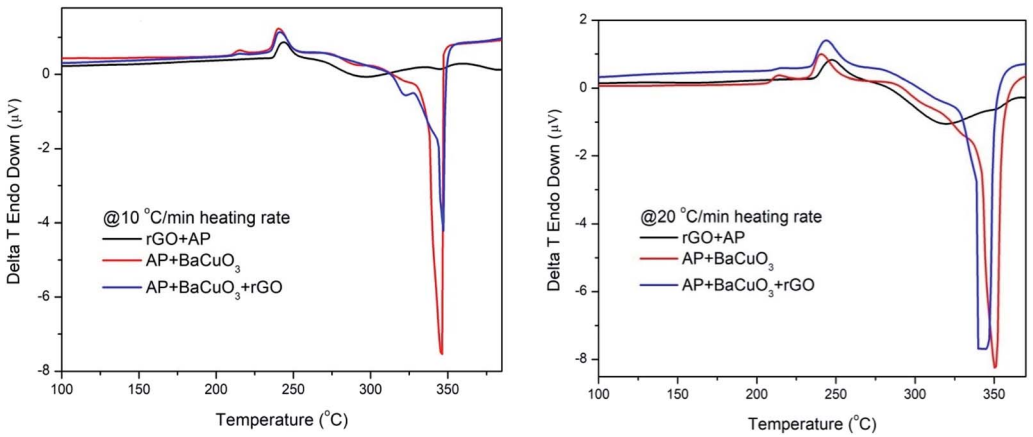

Fig. 5 Catalytic DTA thermographs of rGO + AP, $BaCuO_3$+AP, and rGO + $BaCuO_3$+AP at heating rate of 10 and 20 °C min^{-1}.

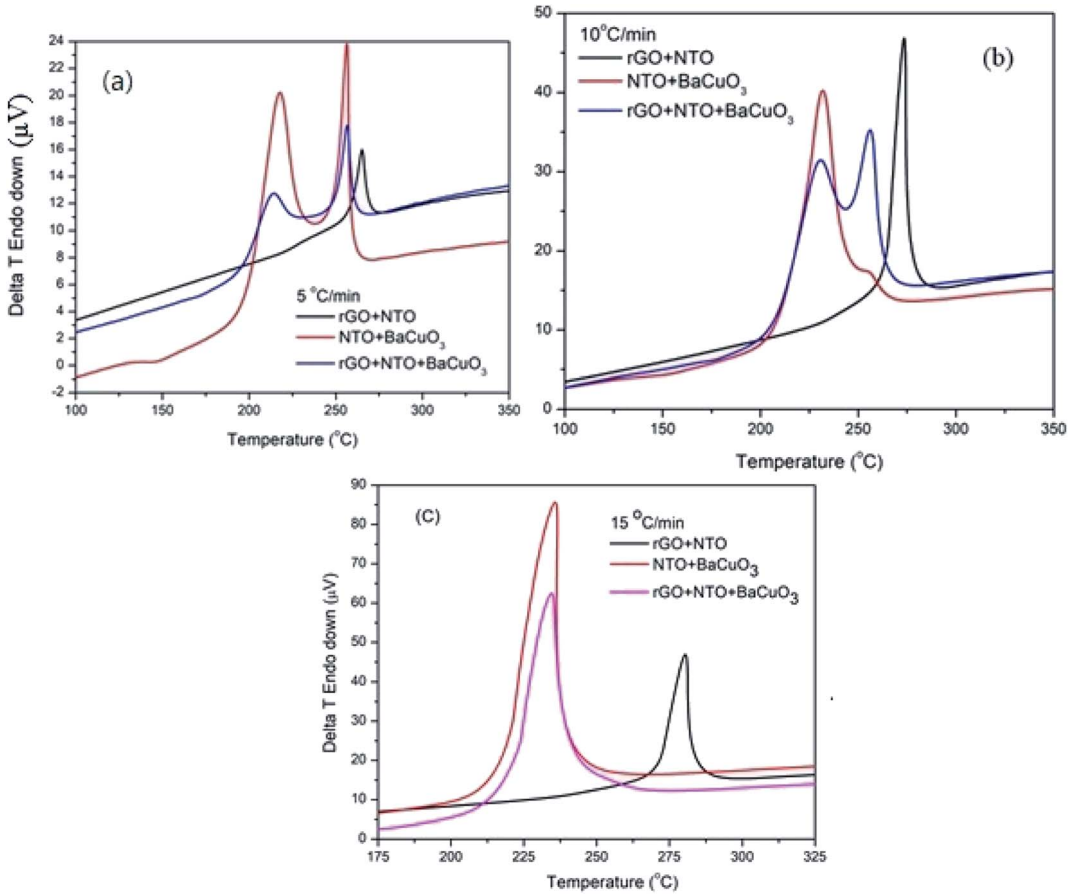

Fig. 6 Catalytic DTA thermographs at heating rates of (a) 5 °C min^{-1}, (b) 10 °C min^{-1}, and (c) 15 °C min^{-1} for rGO + NTO, $BaCuO_3$+NTO, rGO + $BaCuO_3$ + NTO.

provides large adsorption ability[27–30] to facilitate the AP decomposition reaction, thus leading to a large amount of heat being released. Finally, when the mixture rGO + $BaCuO_3$ + AP is heated, the catalysts boost the dissociation of perchlorate ions *via* electron transfer and the adsorption characteristics of the catalysts, thus enhancing the catalytic effect by decreasing the decomposition peak temperature compared with pure AP.

4.6. Thermal analyses for the thermolysis of nitrotriazolone (NTO)

Previous studies have shown that Cu-based perovskite-structured oxides show excellent catalytic activity towards the direct decomposition of nitrogen- and oxygen-containing molecular structures or a decomposition step that includes the formation of NO at high temperature, which then further decomposes into gaseous molecules, which are the most challenging reactions in catalysis.[6]

NTO thermolysis took place in the presence of the rGO and $BaCuO_3$ catalysts at 5, 10, and 15 °C min^{-1} heating rates using DTA analysis, as depicted in Fig. 6. NTO decomposed from 205 to 275 °C, while pure NTO decomposed at around at ~275 °C (Fig. 4). The catalytic decomposition of NTO (Fig. 6) showed that the rGO + NTO decomposition temperature was higher than the two-stage decomposition that took place over the NTO +

Table 1 Thermodynamics and kinetics parameters derived from DTA traces

Samples/parameters	T_p (K)	$\Delta H^{\ddagger}$ (kJ mol^{-1})	$\Delta G^{\ddagger}$ (kJ mol^{-1})	$\Delta S^{\ddagger}$ (J mol^{-1} K^{-1})	E_a (kJ mol^{-1})	ln A
AP	708	158	201	107	147	15.5
AP + rGO	569	112	125	54	95	13.1
AP + $BaCuO_3$	623	120	132	65	102	13.7
rGO + AP + $BaCuO_3$	620	120	132	65	102	13.7
NTO	548	142	179	99	137	14.9
NTO + rGO	546	128	137	68	110	13.9
NTO + $BaCuO_3$	507	111	124	52	94	12.5
rGO + NTO + $BaCuO_3$	509	114	127	58	97	13.1

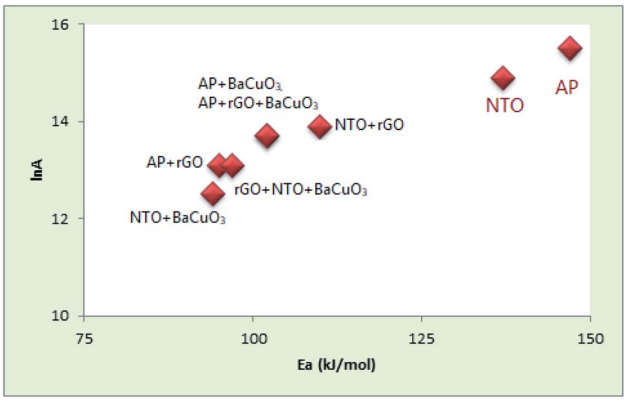

Fig. 7 Kinetics plot of AP and NTO with and without catalyst systems.

$BaCuO_3$ and rGO + $BaCuO_3$ + NTO systems at 5 and 10 °C min^{-1} heating rates. However, at a heating rate of 15 °C min^{-1}, the NTO + $BaCuO_3$ and rGO + $BaCuO_3$ + NTO systems showed a single decomposition peak between 225 and 238 °C. Moreover, the decomposition mechanism of NTO included multiple pathways *via* the production of gaseous products.[31–33]

The energetic decomposition peak temperatures of pure AP, rGO + AP, $BaCuO_3$ + AP, rGO + $BaCuO_3$ + AP, pure NTO, rGO + NTO, $BaCuO_3$ + NTO, and rGO + $BaCuO_3$ + NTO are summarized in Table 1 and the corresponding kinetic data, such as the activation energy and pre-exponential factor, are also incorporated in this table. Further, these data are graphically depicted in Fig. 7.

4.7. Kinetic and thermodynamic studies of AP and NTO

The catalytic activities of rGO, BaCuO3, and rGO + $BaCuO_3$ were further confirmed by the decreased activation energy of AP and NTO in the presence of rGO, $BaCuO_3$, and rGO + $BaCuO_3$. The thermodynamics and kinetics parameters were calculated using the following equations[34–36] for the various systems with and without catalysts, *e.g.*, pure AP, rGO + AP, $BaCuO_3$ + AP, rGO + $BaCuO_3$ + AP, pure NTO, rGO + NTO, $BaCuO_3$ + NTO, and rGO + $BaCuO_3$ + NTO.

$$\ln \frac{\beta}{T_P^2} = \ln \frac{RA_K}{E_K} - \frac{E_K}{R}\frac{1}{T_P} \quad (4)$$

$$\Delta H^{\ddagger} = E_K - RT_P \quad (5)$$

$$\Delta G^{\ddagger} = \Delta H^{\ddagger} - T_P \Delta S^{\ddagger} \quad (6)$$

$$k = A \exp\left(-\frac{E_K}{RT_P}\right) = \frac{K_B T_P}{h} \exp\left(-\frac{\Delta G^{\ddagger}}{RT_P}\right) \quad (7)$$

where T_p is the decomposition peak temperature, K_B is the Boltzmann constant of 1.381×10^{-23} J K^{-1}, h is Plank's constant of 6.626×10^{-34} J s, β is the heating rate, E_a is the activation energy, and A is the pre-exponential factor. The thermodynamics parameters are $\Delta H^{\ddagger}$ (activation enthalpy), $\Delta G^{\ddagger}$ (activation Gibbs free energy), and $\Delta S^{\ddagger}$ (activation entropy).

The E_a values for pure AP and pure NTO are 147 and 137 kJ mol^{-1}, respectively, while the E_a values of rGO + AP, $BaCuO_3$ + AP, rGO + $BaCuO_3$ + AP, rGO + NTO, $BaCuO_3$ + NTO, and rGO + $BaCuO_3$ + NTO are 95, 102, 102, 110, 94, and 97 kJ mol^{-1}, respectively. These are significant results because the decomposition of AP and NTO in the presence of catalysts should be faster than the decomposition of pure AP and NTO, indicating that the thermal decomposition of AP and NTO is accelerated in the presence of rGO and the nano perovskites. The energetic components AP and NTO do not decompose spontaneously. Their initiation required heat (*i.e.*, ΔH). According to the $\Delta H^{\ddagger}$ values in Table 1, pure AP and NTO require more heat to be activated than their compositions with the catalysts rGO, $BaCuO_3$, and rGO + $BaCuO_3$. All of the $\Delta G^{\ddagger}$ are positive values, showing that the decompositions of AP and NTO are not spontaneous, also positive values for $\Delta S^{\ddagger}$ are associated with an increase in the randomness of the system when the activation of the molecules occurs; thus, the lower the S value, the more stable the system. Finally, the thermodynamic results of AP and NTO with and without the catalyst systems were significantly correlated to kinetics studies.

5. Conclusions

rGO catalysts were successfully synthesized *via* thermal treatment while the nanosized perovskite oxide $BaCuO_3$ was also successfully prepared *via* a wet chemical citrate-EDTA method. The catalytic effect on the thermolysis of AP and NTO concluded that rGO was an active catalyst for AP compared to NTO, while the $BaCuO_3$ and rGO + $BaCuO_3$ catalysts were active toward NTO compared to AP in terms of decomposition peak temperature. The enhanced catalytic activity of rGO for AP thermolysis was attributed to the fast electron acceptor behavior of rGO. However, the excellent catalytic performance of the perovskite-based catalyst toward NTO thermolysis was attributed to the synergistic effect of rGO + $BaCuO_3$ and the availability of the large absorption surface of $BaCuO_3$. This makes the rGO and $BaCuO_3$ nanomaterials promising catalysts for AP- and NTO-based energetic materials or chemical propulsion systems.

Author contributions

The author contributions are as follows: Pragnesh N. Dave – conceptualization, project administration, funding acquisition, resources, visualization, writing – review and editing, and supervision; Riddhi Thakkar – methodology, investigation, data curation, validation, and writing – original draft; Ruksana Sirach – methodology, investigation, and formal analysis.

Conflicts of interest

There are no conflicts to declare.

Acknowledgements

The authors are grateful to the Department of Chemistry, Indukaka Ipcowala Center for Interdisciplinary Studies in Science and Technology (IICISST), and the Department of Physics, Sardar Patel University, Vallabh Vidyanagar, Gujarat, India, for providing various instrumental facilities such as

Raman spectroscopy, XRD, UV-vis spectroscopy, and thermal analyses. The authors are also thankful to SICART (Sophisticated Instrumentation Centre for Applied Research and Testing) for providing the FE-SEM instrument facility. The authors RT and RS are grateful to DST (SR/NM/NT-1014/2016 (G)) for the Junior Research Fellowship and Research Associate Fellowship, respectively.

References

1 D. Trache, T. M. Klapötke, L. Maiz, M. Abd-Elghany and L. T. DeLuca, *Green Chem.*, 2017, **19**, 4711–4736.
2 M. Sieradzka, C. Ślusarczyk, W. Biniaś and R. Fryczkowski, *Coatings*, 2021, **11**, 166.
3 A. Jabbar, G. Yasin, W. Q. Khan, M. Y. Anwar, R. M. Korai, M. N. Nizam and G. Muhyodin, *RSC Adv.*, 2017, **7**, 31100–31109.
4 T. Chen, Y. Hu, C. Zhang and Z. Gao, *Def. Technol.*, 2021, **17**, 1471–1485.
5 J. A. Ciller, F. J. Serna and J. R. Quintana, *J. Energ. Mater.*, 1992, **10**, 251–265.
6 N. F. Atta, A. Galal and E. H. El-Ads, *Perovskite Materials-Synthesis, Characterisation, Properties, and Applications*, 2016, pp. 107–151.
7 R. R. Sirach and P. N. Dave, *Chem. Heterocycl. Compd.*, 2021, **57**, 720–730.
8 S. Hanafi, D. Trache, W. He, W. X. Xie, A. Mezroua and Q. L. Yan, *Thermochim. Acta*, 2020, **692**, 178747.
9 A. Ezzahi, B. Manoun, A. Ider, L. Bih, S. Benmokhtar, M. Azrour and P. Lazor, *J. Mol. Struct.*, 2011, **985**, 339–345.
10 E. Abdul and R. Assirey, *Saudi Pharm. J.*, 2019, **27**, 817–829.
11 A. Rezanezhad, E. Rezaie, L. Saleh, A. Hajalilou, E. Abouzarilotf and N. Arsalani, *Electrochim. Acta*, 2020, **335**, 135699.
12 W. Wang and D. Zhang, *RSC Adv.*, 2018, **8**, 32221–32230.
13 A. T. Smith, A. Marie, S. Zeng, B. Liu and L. Sun, *Nano Mater. Sci.*, 2019, **1**, 31–47.
14 F. Yin, S. Wu, Y. Wang, L. Wu, P. Yuan and X. Wang, *J. Solid State Chem.*, 2016, **237**, 57–63.
15 W. C. Oh and F. J. Zhang, *Asian J. Chem.*, 2011, **23**, 875–879.
16 K. Lysien, A. Stolarczyk and T. Jarosz, *Materials*, 2021, **14**, 6657.
17 R. K. Parida, D. K. Pattanayak, B. Mohanty, N. C. Nayak and B. N. Parida, *J. Adv. Dielectr.*, 2019, **9**, 1950004.
18 O. Domínguez, *J. Energ. Mater.*, 2019, 1–12.
19 Y. Hu, B. Tao, F. Shang, M. Zhou and D. Hao, *Appl. Surf. Sci.*, 2020, 145849.
20 J. M. Sailaja, N. Murali, S. J. Margarette, N. K. Jyothi, K. Rajkumar and V. Veeraiah, *S. Afr. J. Chem. Eng.*, 2018, **26**, 61–69.
21 P. Vázquez-Sánchez, m. A. Rodríguez-Escudero, F. J. Burgos, I. Llorente, O. Caballero-Calero, M. M. González and M. C. García-Alonso, *J. Alloys Compd.*, 2019, **800**, 379–391.
22 I. K. Moon, J. Lee, R. S. Ruoff and H. Lee, *Nat. Commun.*, 2010, **1**, 1–6.
23 W. Haron, A. Wisitsoraat, U. Sirimahachai and S. Wongnawa, *Songklanakarin J. Sci. Technol.*, 2018, **40**, 484–491.
24 I. Notingher, *Characterisation using Raman micro-spectroscopy*, Woodhead Publishing, 2007, pp. 248–266, DOI: **10.1533/9781845693817.1.248**.
25 P. Dave, R. Thakkar, R. Sirach, M. P. Deshpande and S. Chaturvedi, *J. Electron. Mater.*, 2021, 1–8.
26 W. Wang and D. Zhang, *RSC Adv.*, 2018, **8**, 32221–32230.
27 Y. Hu, B. Tao, F. Shang, M. Zhou, D. Hao, R. Fan, D. Xia, Y. Yang, A. Pang and K. Lin, *Appl. Surf. Sci.*, 2020, **513**, 145849.
28 S. Jain, V. H. Khire and B. Kandasubramanian, *Propellants, Explos., Pyrotech.*, 2019, **44**, 505–512.
29 S. Kumar, A. Vinu, J. Subrt, S. Bakardjieva, S. Rayalu, Y. Teraoka and N. Labhsetwar, *Catal. Today*, 2012, **198**, 125–132.
30 Z. X. Wei, Y. Q. Xu, H. Y. Liu and C. W. Hu, *J. Hazard. Mater.*, 2009, **165**, 1056–1061.
31 D. S. Viswanath, T. K. Ghosh and V. M. Boddu, *Emerging energetic materials: Synthesis, physicochemical, and detonation properties*, Springer, Dordrecht, 2018.
32 G. Singh, I. P. S. Kapoor, S. K. Tiwari and P. S. Felix, *J. Hazard. Mater.*, 2001, **81**, 67–82.
33 G. Yang, F. Nie, J. Li, Q. Guo and Z. Qiao, *J. Energ. Mater.*, 2007, **25**, 35–47.
34 Y. Wang, X. Song, D. Song, L. Liang, C. An and J. Wang, *J. Hazard. Mater.*, 2016, **312**, 73–83.
35 S. Sahani, T. Roy and Y. C. Sharma, *J. Cleaner Prod.*, 2019, **237**, 117699.
36 J. Akhavan, *The chemistry of explosives*, 2007, pp. 74–102.